Tellus (1990), *42A*, 14–27

Empirical modeling of extra-tropical cyclone vorticity fluxes

By WERNER METZ, *Meteorological Institute, University of München, Theresienstraße 37, D-8000 München 2, FRG*

(Manuscript received 15 November 1988; in final form 6 March 1989)

ABSTRACT

The relationship between the slow components of the hemispheric barotropic flow and the barotropic effects on the flow due to the presence of extra-tropical cyclones is investigated by establishing multivariate regression models. These regression models are formulated in terms of the modes that are obtained from a canonical correlation analysis between the two variables. 8 winters of hemispheric spectral observations are used for the analysis which is carried out on the basis of unfiltered time series for the barotropic streamfunction and the eddy effects. It turns out that the regression models exhibit some local skill (up to 30%) over the Atlantic sector to predict the eddy effects in terms of the planetary streamfunction. Furthermore, it is found that this skill is mainly associated with the largest planetary scales of the eddy effects. The dynamical flow regimes that contribute to this skill are also evaluated. It is found that they comprise episodes of Atlantic blocking as well as cases when the flow over the Atlantic is governed by an anomalous zonal jet. The characteristic time-scale for those episodes is estimated as about 10 days.

1. Introduction

The interaction between extra-tropical cyclones and the low-frequency, large-scale components of the atmospheric flow has received much interest in recent years. Dole (1986b) has given evidence that the stormtracks (as represented by anomalous band-pass eddy variances) over the Atlantic and Pacific oceans are systematically deflected from their normal positions during episodes of persistent 500 mb geopotential height anomalies. A similar finding has been made by Mullen (1987), who considered cases of observed and GCM simulated blocking highs. He has also shown that the composite transient eddy vorticity flux divergences at upper levels dominate the eddy heat flux divergences, tending to cause the blocking pattern to retrograde, and opposing any tendency for the block to be advected downstream by the time-mean wind. This view is supported by other studies, e.g., Austin (1980), Illari and Marshall (1983), Shutts (1986) or Holopainen and Fortelius (1987).

Adopting an entirely different point of view, Egger and Schilling (1983, 1984) have hypothesized that the role of extra-tropical cyclone-scale eddies for the low-frequency components of planetary atmospheric flow can be, to first order, described in terms of a stochastically driven dissipative flow. To explore this possibility, they forced a simple quasi-geostrophic, barotropic low-order model by the eddy vorticity flux convergences due to cyclone-scale eddies. Hereby, only the largest planetary scales of the flux divergences were considered, corresponding to the truncation rule of the low-order model. In accordance with the stochastic forcing concept, the eddy-induced fluxes were prescribed independently of the instantaneous state of the large-scale flow, whereby either being computed, using observed data, or being parameterized in terms of first-order autoregressive processes. In these experiments, a considerable agreement between the variability in the model and the observed low-frequency variance was achieved. It has also been found (Metz, 1987) that the performance of the model is significantly improved, if care is taken in considering the spatial structure of the observed vorticity flux convergences. This was accomplished by expanding the eddy forcing into its EOFs, and representing the principal component time series by Markov models. The stochastic forcing concept has also been applied to the blocking problem (Metz, 1986), whereby it exhibited some skill with respect to the simulation of Atlantic blocking episodes. However, because of the above-mentioned evidence of a local relationship between cyclone-scale eddies and low-frequency oscillation periods from 2.5 to 6 days, streamfunctions are obtained from 8 winters (1979/80–1986/87) of ECMWF observations. Using these data, time series of the barotropic mode (in a two-level model formulation) of the cyclone-scale eddy vorticity flux convergences are evaluated. The statistical analysis in the present paper will be carried out using the unfiltered time series of the barotropic streamfunction and the eddy effects. The reason for not using low-pass filtered data (as in M89) was that, as discussed by Dole (1986a), the transitions between different large-scale flow regimes occur rather rapidly, so that low-pass filtering might cause the loss of statistically important information. Furthermore, the number of effective degrees of freedom associated with the analysis will be considerably larger than for low-pass filtered data. However, as we will show, the modes obtained in this study are essentially similar, although not identical, to the modes obtained in M89.

The relationship between the large-scale flow and the largest planetary scales (e.g., zonal wavenumbers $m \leqslant 4$) of the eddy flux convergences is of particular relevance with respect to the possibility of using the above-mentioned regression models as a parameterization of cyclone-scale eddy effects in low-order models. To examine this relationship, a separate analysis will be carried out using a highly truncated representation of the eddy effects.

The data set and the data manipulations, which include expansion into principal components, as described in Section 2. The statistical method is discussed in Section 3. The results are presented in Section 4 and are discussed in Section 5.

2. Data

2.1. Basic data

The basic data set are 8 winters (1979/80–1986/87) of ECMWF geopotential height analyses. Each winter starts on 20 November and comprises 110 daily observations. As described in M89, the geopotential heights are converted to streamfunctions and the barotropic ψ and baroclinic τ modes of the latter are computed. In particular, ψ and τ are represented in the form of complex spherical harmonic coefficients with a triangular truncation at total wavenumber $n = 21$. Because the analysis deals only with the northern hemisphere, only the odd spectral modes (i.e., $n - |m| = \text{odd}$) are retained (121 complex coefficients).

2.2. Computation of eddy forticity flux convergences

The cyclone-scale eddies (ψ_B, τ_B) are defined by applying a band-pass filter (Blackmon and Lau, 1980; 2.5–6 days) to ψ and τ. Due to the width of the filter, this procedure causes the loss of 10 observations at the two ends of each winter time series. The barotropic vorticity flux convergences due to these cyclone-scale eddies are then computed in the domain of complex spherical harmonics (using a two-level model formulation) according to the spectral equivalent of:

$$\mathscr{F} = -J(\psi_B, \nabla^2 \psi_B) - J(\tau_B, \nabla^2 \tau_B), \tag{1}$$

whereby the method of spectral interaction coefficients is used to evaluate the Jacobians.

Following M89, the annual cycle and the mean are removed from the time series of ψ and $\mathscr{F}$ for each winter separately. Fig. 1a illustrates the standard deviation of $\mathscr{F}$ for the 8 winter samples, where (as in M89) it is displayed in the form of associated streamfunction tendencies $\nabla^2 \mathscr{F}$. One can see that $\mathscr{F}$ has large variability over the oceans (and over North America), and the Pacific maximum has only about $\frac{3}{4}$ of the variance of the Atlantic maximum. The positions and the structure of the extremes in Fig. 1a are very similar to those of the standard deviation of the low-pass components (periods from 10 days to 3 months) of $\mathscr{F}$, which is shown in Fig. 1b of M89. A comparison of the magnitudes indicates that only about $\frac{1}{2}$ of the total intraseasonal variance of $\mathscr{F}$ is due to its low-pass components, which is

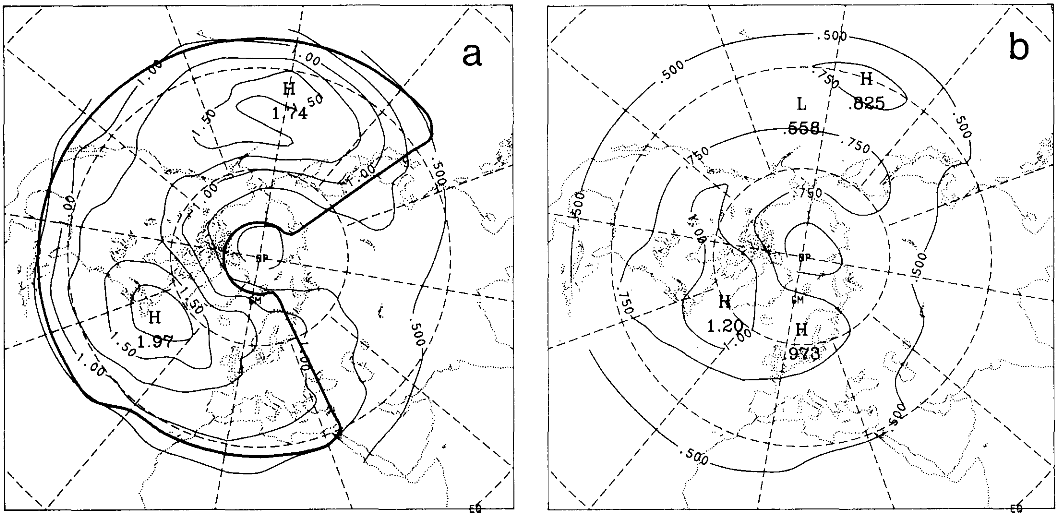

Fig. 1. Intraseasonal standard deviations of (a) $\nabla^{-2}\mathscr{F}$ and (b) $\nabla^{-2}\mathscr{F}_{R_4}$. Contour intervals are $0.25 \cdot 10^6$ m^2 s^{-1} day^{-1}. Also shown in (a) is the reference area (bold line) used for the statistical tests (see Appendix).

much less than what one obtains for, e.g., geopotential height data (e.g., Blackmon, 1976).

As indicated in Section 1, we are particularly interested in the largest planetary scales of $\mathscr{F}$. Therefore, a subtruncation $\mathscr{F}_{R_4}$ of $\mathscr{F}$ is defined in terms of a rhomboidal truncation where only those spectral coefficients with zonal wavenumbers $m \leqslant 4$ and total wavenumbers $n \leqslant |m| + 11$ are retained (however, $n - |m| =$ odd). An inspection of the standard deviation obtained for $\mathscr{F}_{R_4}$ (Fig. 1b) shows that the variance level is generally lower (about 0.4) than that for the total eddy effects. Furthermore, the Atlantic maximum is shifted northward (with respect to Fig. 1a). The Pacific maximum, however, is severely distorted and has only about $\frac{1}{2}$ of the variance of the Atlantic maximum. This indicates that large-scale effects of $\mathscr{F}$ are more important over the Atlantic sector than over the Pacific.

2.3. *Principal components*

As discussed in M89, the time series of ψ and $\mathscr{F}$ are firstly expanded into their principal components and a certain number of these is then used as input data for the canonical correlation analysis. For this purpose, a conventional real EOF analysis is performed in the spectral domain in which the complex spherical harmonic coefficients are transformed to their real equivalents, i.e., the zonal variations are represented by sine and cosine coefficients.

Table 1 illustrates the principal component expansions of ψ that have been obtained for the winter data. The first 10 eigenvalues (out of a total number of 231) of ψ represent 51.3% of the total variance. All eigenvalues are degenerate as can be seen from their empirical standard deviations. The number of effective degrees of freedom that is associated with the principal components is 224.1, corresponding to a time of 3.9 days ($1/e$ time, see Appendix) between independent samples. The leading principal components represent persistent processes as can be inferred form their large $1/e$ values of about 2 weeks. This persistence decreases to about 1 week for the 2nd half of the selected principal components.

The principal component expansion of $\mathscr{F}$ (Table 2) converges much more slowly than that of ψ (the first 10 representing only 28.1% of total variance; 23 components are needed to represent 50%). In this case, all data (720 days) must be considered as independent, which is also reflected in the persistence values of the principal components. This indicates that $\mathscr{F}$, as the result of a nonlinear operation (cf. eq. (1)), appears to

Table 1. *Variance (%) explained by the first 10 eigenvalues obtained for the EOF analysis of ψ together with their empirical standard deviations*

No.	Variance (%)	$1/e$ time (days)
1	8.3 ± 0.8	14.5
2	7.6 ± 0.7	14.9
3	6.4 ± 0.6	11.7
4	5.7 ± 0.5	9.8
5	5.2 ± 0.5	9.3
6	4.3 ± 0.4	5.2
7	3.8 ± 0.4	6.1
8	3.6 ± 0.3	7.1
9	3.3 ± 0.3	6.9
10	3.1 ± 0.3	7.7

The total sample size is 880 days, and 224.1 effective degrees of freedom were used to evaluate the standard deviations. Also shown (column 2) are the $1/e$ values of the autocorrelation functions for the principal component time series.

Table 2. *As Table 1, but for EOF analysis of $\mathscr{F}$ (spectral truncation T21)*

No.	Variance (%)	$1/e$ time (days)
1	4.0 ± 0.2	1.3
2	3.4 ± 0.2	1.1
3	3.3 ± 0.2	0.6
4	2.9 ± 0.2	0.7
5	2.9 ± 0.2	0.8
6	2.5 ± 0.1	0.5
7	2.4 ± 0.1	0.5
8	2.3 ± 0.1	0.4
9	2.2 ± 0.1	0.4
10	2.2 ± 0.1	0.0

Total sample size and equivalent degrees of freedom: 720.

Table 3. *As Table 1, but for EOF analysis of $\mathscr{F}_{R_4}$*

No.	Variance (%)	$1/e$ time (days)
1	14.5 ± 0.9	1.3
2	12.0 ± 0.7	1.5
3	11.6 ± 0.7	1.4
4	9.1 ± 0.6	1.5
5	7.4 ± 0.4	1.1
6	6.9 ± 0.4	1.2
7	6.4 ± 0.4	1.2
8	5.5 ± 0.3	1.0
9	4.0 ± 0.2	1.1
10	3.5 ± 0.2	1.2

Total sample size is 720 days and empirical standard deviations are based on 551.2 degrees of freedom.

contain a lot of high-frequency noisy components.

The statistical characteristics of the principal component expansions of the low-order representation $\mathscr{F}_{R_4}$ of $\mathscr{F}$ can be inferred from Table 3. Due to the planetary truncation, the total number of principal components is reduced to 35, where the first five sum up to 55% of the total variance. As one can infer from the $1/e$ values, the principal components are still rather noisy, so that the effective number of degrees of freedom is only little reduced (551). Thus, the empirical standard deviation associated with the eigenvalues is still rather small, and in particular, the 1st, the 2nd and 3rd taken together, and the 4th eigenvalue are likely to be distinct from one another.

3. Method

The statistical method used in the present study is a multivariate regression based on canonical correlation analysis. In particular, multivariate regression models will be developed to predict the cyclone-scale eddy vorticity flux convergences $\mathscr{F}$ in terms of the instantaneous state of the hemispheric flow ψ.

3.1. Canonical correlation analysis

The canonical correlation analysis (CCA) technique, which goes back to Hotelling (1936), is described in detail in M89 (cf. also Barnett and Preisendorfer, 1987), so that only a brief discussion of its basic features will be presented here. Basically, the CCA selects a pair of spatial patterns in 2 space-time dependent sets of variables such, that the (time dependent) pattern amplitudes are optimally correlated. Mathematically, the patterns are determined by solving a coupled eigenvalue problem (cf. M89, Appendix A). The method gives not just one pair of patterns but a hierarchy of pairs, each associated with a certain eigenvalue λ_j^2. This eigenvalue turns out to be just the squared correlation between the pattern amplitude time series. The latter are termed canonical variates and are denoted by U_j and V_j, respectively, the subscript j indicating the relation to a particular eigenvalue λ_j^2. Furthermore, a particular eigensolution is called a canonical mode. The canonical modes are, for convenience, ordered with respect to the magnitude of their eigenvalues λ_j^2.

It is highly advisable to apply a reduction of the data space prior to the CCA. This is most easily accomplished by projecting the data onto their principal components and then retaining for the analysis only a limited number of them. In particular, subsets (N_ψ, N_F) of the principal component expansions of ψ and $\mathscr{F}(\mathscr{F}_{R_4})$ are used as input data for the CCA. The significant (cf. below) canonical modes, obtained from a particular choice of N_ψ and N_F, are then used to build regression models, as will be described in the following. In particular, the total number of canonical modes obtained is given by $\min(N_\psi, N_F)$. In order to visualize in geometrical space the patterns of ψ and $\mathscr{F}$ that are associated with a particular canonical mode, canonical maps (cf. M89) are constructed according to:

$$G_j(\lambda, \varphi) = \overline{X(\lambda, \varphi \cdot t)\, U_j(t)}. \tag{2}$$

Here, $X(\lambda, \varphi, t)$ denotes the time series of, e.g., ψ at the gridpoint (λ, φ) and U_j represents the time series of the canonical variate U_j and V_j, respectively. The pattern shown in a canonical map is the spatial distribution of the local covariances between the canonical variates and the original data in gridpoint space. Furthermore, because U_j and V_j have unit variance by definition (cf. M89, Appendix A), the pattern displayed in a canonical map has the same dimension as the physical variable under consideration. The significance of the canonical modes is determined by testing the canonical maps; the procedure applied for that purpose is described in the Appendix.

3.2. Regression models

The canonical modes are used to build regression models for the prediction of $\mathscr{F}$ in terms of ψ. Thereby, we follow the approach described by Barnett and Preisendorfer (1987). The first step consists of expanding the detrended complex spectral vectors $\mathbf{\Psi}$, $\boldsymbol{F}$ in terms of the canonical modes. If J significant modes have been obtained, these expansion are written:

$$\mathbf{\Psi}(t) = \sum_{j=1}^{J} \mathbf{\Pi}_j\, U_j(t) + \varepsilon_{\mathbf{\Psi}}(t), \tag{3}$$

$$\boldsymbol{F}(t) = \sum_{j=1}^{J} \mathbf{\Gamma}_j\, V_j(t) + \varepsilon_{\mathrm{F}}(t) = \hat{\boldsymbol{F}}(t) + \varepsilon_{\mathrm{F}}(t), \tag{4}$$

where $\mathbf{\Pi}_j$ and $\mathbf{\Gamma}_j$ are complex pattern vectors representing the structure of the canonical modes in spectral domain and $\hat{\boldsymbol{F}}$ denotes the resolved part of $\boldsymbol{F}$. Because the canonical variates U_j, V_j are orthogonal in time, i.e.,

$$\overline{U_i U_j} = \overline{V_i V_j} = \delta_{ij}, \quad \overline{U_i V_j} = \lambda_i \delta_{ij}. \tag{5}$$

Least squares estimates for the $\mathbf{\Pi}_j$ and $\mathbf{\Gamma}_j$ are given by:

$$\mathbf{\Pi}_j = \overline{\mathbf{\Psi}(t)\, U_j(t)}, \tag{6}$$

$$\mathbf{\Gamma}_j = \overline{\boldsymbol{F}(t)\, V_j(t)}. \tag{7}$$

The pattern vectors $\mathbf{\Pi}_j$ and $\mathbf{\Gamma}_j$ can be considered as spectral equivalents of the canonical maps (2). In contrast to the canonical projection vectors (cf. M89, Appendix), the vectors $\mathbf{\Pi}_j$ and $\mathbf{\Pi}_j$ are not unitary (i.e., complex orthogonal).

The regression model building is based on the concept that the time series of the U_j (i.e., only the part of ψ resolved by the canonical modes) be used to predict $\mathscr{F}$. Thus, the part of $\mathscr{F}$ that is resolved by the canonical modes $\hat{\boldsymbol{F}}$ must be expressed in terms of the U_j:

$$\hat{\boldsymbol{F}}(t) = \sum_{j=1}^{J} \boldsymbol{X}_j\, U_j(t) + \varepsilon(t), \tag{8}$$

where J again indicates the number of significant canonical modes used. The unknown vectors $\boldsymbol{X}_j$ can be determined by the least squares method. One gets:

$$\boldsymbol{X}_j = \overline{\hat{\boldsymbol{F}} U_j} = \overline{U_j(t) \sum_{k=1}^{J} \mathbf{\Gamma}_k V_k(t)} = \mathbf{\Gamma}_j \lambda_j, \tag{9}$$

where use has been made of (4) and (5). Thus, the final regression model is written:

$$\tilde{\boldsymbol{F}}(t) = \sum_{j=1}^{J} \mathbf{\Gamma}_j \lambda_j\, U_j(t). \tag{10}$$

Here, the impact of the canonical correlation coefficient λ_j is evident.

3.3. Significance and skill

The global skill of the regression model (10) with respect to that part of $\mathscr{F}$, which is resolved by the canonical modes (cf. eq. (4)), is given by:

$$S_c = \frac{\overline{\tilde{\boldsymbol{F}}\tilde{\boldsymbol{F}}^*}}{\overline{\hat{\boldsymbol{F}}\hat{\boldsymbol{F}}^*}} = \left\{\sum_{j=1}^{J} |\mathbf{\Gamma}_j|^2 \lambda_j^2\right\} \Big/ \left\{\sum_{j=1}^{J} |\mathbf{\Gamma}_j|^2\right\}. \tag{11}$$

However, it will be more informative to evaluate the skill and the significance of the regression (10) with respect to the total observed variance of $\mathcal{F}$. For that purpose, one can operate either in wavenumber space or in gridpoint space. Because the variability of $\mathcal{F}$ is characterized by significant regional maxima (cf. Fig. 1), an evaluation in gridpoint space appears to be the more appropriate.

In particular, we proceed as follows. At each gridpoint of a regular latitude–longitude grid (5° by 10°) time series of $\tilde{\mathcal{F}}$ are recovered using (10). The local significance of the regression model is then evaluated by testing the lag zero correlation:

$$c_{\mathrm{L}} = \frac{\overline{\mathcal{F}'(\lambda, \varphi, t)\,\tilde{\mathcal{F}}'(\lambda, \varphi, t)}}{(\overline{\mathcal{F}'^2}\;\overline{\tilde{\mathcal{F}}'^2})^{1/2}}. \tag{12}$$

The test statistic used is described in the Appendix.

The global significance of the regression is then estimated by comparing the area which is covered by significant correlations with a reference area (cf. Appendix). The local skill at individual gridpoints is evaluated according to:

$$S_{\mathrm{L}}(\lambda, \varphi) = 1 - \left.\frac{\overline{(\mathcal{F} - \tilde{\mathcal{F}})^2}}{\overline{\mathcal{F}'^2}}\right|_{\lambda, \varphi}. \tag{13}$$

Finally, an estimate of the global skill of the regression can be obtained as a weighted average of the significant local skill values.

4. Results

4.1. Total eddy effects

4.1.1. Canonical correlation analysis. As outlined above, certain numbers N_ψ, N_{F} of principal components of ψ and $\mathcal{F}$ (cf. Subsection 2.3) have to be selected for the CCA. To determine the truncation points of the expansions, one could use, e.g., the principal component selection rules (Preisendorfer et al., 1981). Another possibility would be to evaluate confidence intervals for the EOF eigenvalues by means of a Monte-Carlo technique (Metz, 1986). However, it has been shown in M89 that the structure of the significant CCA modes is not particularly sensitive to the specific truncation points used. In principle, retaining too many components yields perfectly matched patterns, but, with very little skill. At the other extreme, statistically significant information may be lost if too few components are retained. Therefore, we follow the guide lines of M89 and use $N_{\mathrm{F}} = 18$ (corresponding to 42.7% explained variance) principal components of $\mathcal{F}$ and $N_\psi = 10$ (51.3%) components of ψ. We have also tested other truncation points, but it turns out that, as in M89, the analysis is not particularly sensitive to the choice of the truncation point, provided a reasonable fraction of explained variance is retained.

The canonical eigenvalues obtained from the CCA are shown in Table 4. These eigenvalues represent the skill that is associated with a linear regression between the U_j and the V_j of one particular canonical mode. One finds that (as has to be expected) the leading eigenvalues in Table 4 are smaller than those which were obtained in M89 using low-pass filtered data in M89. Because the first 2 eigenvalues of Table 4 are separated from the remainder, they are the most promising candidates to be associated with significant canonical modes. As we have discussed above, the significance of a canonical mode is ascertained by testing the significance of the canonical maps. These significant canonical modes will then be used for the construction of the regression model. However, before going on to the regression problem, let us first discuss the canonical maps of ψ and $\mathcal{F}$ that are associated with the first two canonical modes.

Table 4. *Eigenvalues obtained for the canonical correlation analysis of ψ and $\mathcal{F}$ (column 1) and of ψ* and $\mathcal{F}_{R_4}$ *(column 2)*

No.	$\psi \leftrightarrow \mathcal{F}$ (51.3%/42.7%)	$\psi \leftrightarrow \mathcal{F}_{R_4}$ (48.2%/47.2%)
1	0.2117	0.2122
2	0.1925	0.1231
3	0.1331	0.1047
4	0.0909	0.0525
5	0.0728	
6	0.0614	
7	0.0494	
8	0.0242	
9	0.0205	
10	0.0133	

Also indicated is the % of variance that is explained by the number of principal components used for the CCA. See text for further explanations.

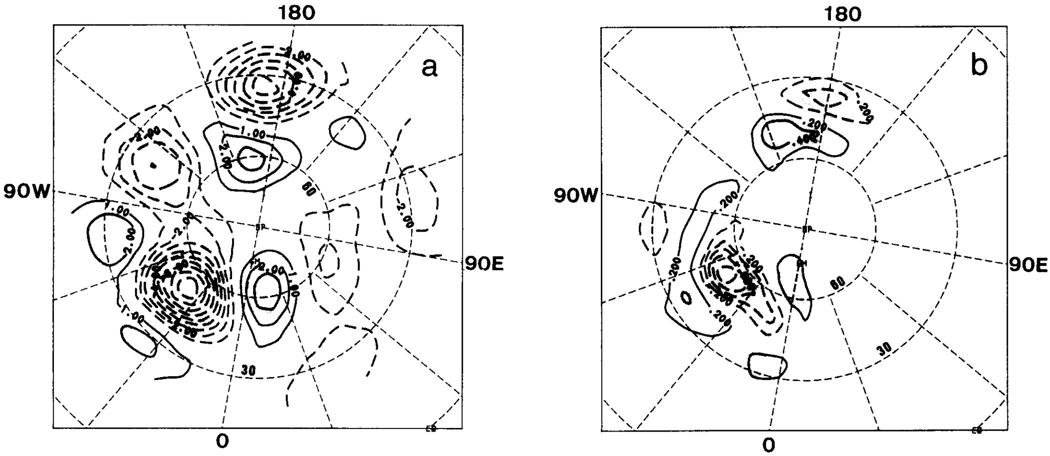

Fig. 2. Canonical maps for (a) ψ and (b) $\nabla^{-2}\mathscr{F}$ associated with the first canonical mode of Subsection 4.1.1. Contour intervals are $1 \cdot 10^6$ m^2 s^{-1} (a) and $0.2 \cdot 10^6$ m^2 s^{-1} day^{-1} (b); zero lines are suppressed. Significant areas are shaded.

The canonical maps (cf. eq. (2)) obtained for ψ and $\nabla^{-2}\mathscr{F}$ for the first canonical mode are shown in Figs. 2a, b. The two patterns are statistically significant, the fractional areas of significant gridpoints being 0.33 and 0.16, respectively. The structure of the streamfunction pattern is rather similar to that obtained for the low-pass filtered case in M89 as CCA mode α. However, a striking difference exists insofar as the pattern of Fig. 2a has its largest amplitudes over the Atlantic, while the CCA mode α (cf. M89, Fig. 3a) had its largest amplitudes over the Pacific. The associated pattern of $\nabla^{-2}\mathscr{F}$ (Fig. 2b) is strongest over the Atlantic, too, and has little similarity to the corresponding pattern of the CCA mode α; however, it is similar over the Atlantic to the CCA mode β of M89. Furthermore, the $\nabla^{-2}\mathscr{F}$ pattern for the second canonical mode (Fig. 3b), being also statistically significant (14% of area), compares well over the Pacific sector with the CCA mode α pattern of M89. The ψ pattern (Fig. 3a), which is also significant (23% of area), is dominated by a large amplitude anomaly over the west coast of North America. However, this pattern bears no similarity to either of the patterns obtained in M89. Thus, while the $\nabla^{-2}\mathscr{F}$ patterns obtained in this analysis and in M89 are rather similar, however, with interchanged ranking, the associated flow patterns are differently arranged by the CCA for the unfiltered and the low-pass filtered case.

As discussed in M89, one should keep in mind that the patterns shown in the canonical maps are of statistical origin and may not be straightforwardly interpreted in terms of large-scale weather regimes. This argument becomes more clear, if one inspects the time series of the canonical variates U_j and V_j, which are shown in Fig. 4 for the case of the first canonical mode. The U_1 curve (bold), representing the degree of the instantaneous projection of the atmospheric flow onto the canonical map of Fig. 2a, is characterized by rather slow oscillations with little superimposed high-frequency noise. An estimate of the $1/e$ time for this time series is about 10 days. In contrast, the V_1 curve, representing the eddy effects, is dominated by high-frequency noise, its estimated $1/e$ time being 1.2 days. However, it contains also a slow component parallel to the U_1 curve, and it is basically this slow component which gives rise to the correlation (0.46) between the two curves. Now, returning to the above argument, one can see that only during relatively few episodes do the U_1 and V_1 curves match closely with large amplitudes. So, dynamical situations which compare well with the patterns of Fig. 2a must be considered to be relatively rare events and thus, many other

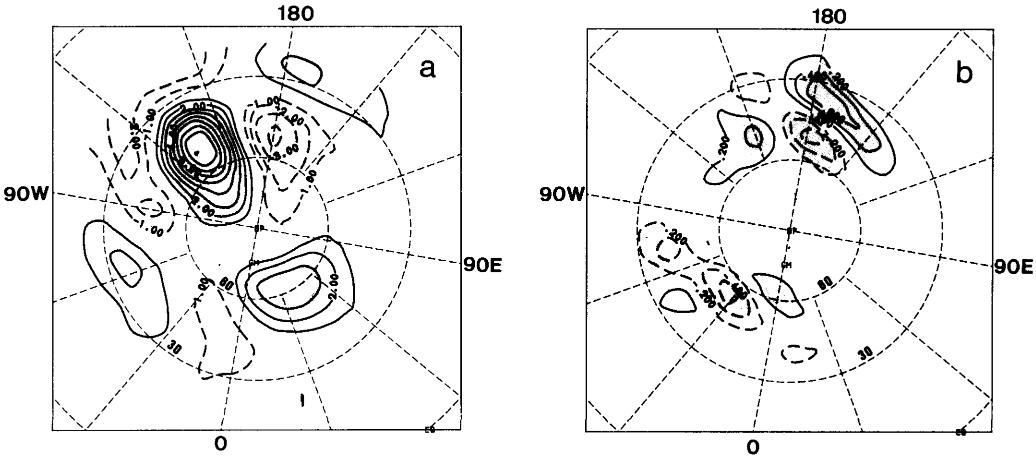

Fig. 3. As Fig. 2, but for the second canonical mode of Subsection 4.1.1.

different situations, that project only partially onto the canonical modes also contribute to the statistical origin of patterns. We shall come back to this point in Section 5.

4.1.2. Regression. We shall now use the two canonical modes, discussed above, to build the multivariate regression model following the procedure described in Subsection 3.2. The first step consists of computing the complex pattern vectors $\boldsymbol{\Gamma}_j$ (cf. eq. (7)) which govern the projection of the observed cyclone-scale eddy vorticity flux convergences $\mathscr{F}$ onto the canonical modes. The second step in the regression procedure consists of recovering the regression estimates according to (10) by using the pattern vectors $\boldsymbol{\Gamma}_j$ and the time series of the U_j for $j = 1, 2$ (cf. Fig. 4). This regression yields time series of complex spherical harmonic coefficients $\tilde{\boldsymbol{F}}$.

As outlined in Subsection 3.2, the significance and the skill of the regression model will be evaluated in gridpoint space. For that purpose, a time series of regression maps is evaluated by recovering gridpoint values $\tilde{\mathscr{F}}$ from the spectral $\tilde{\boldsymbol{F}}$ coefficients. These regression maps are then verified against the corresponding observed data maps by testing at each gridpoint the correlations (12) against twice their empirical standard deviations S_R (cf. eq. (A1), Appendix). As discussed in the Appendix, the evaluation of S_R requires the characteristic lag 1 autocorrelations for $\mathscr{F}$ and $\tilde{\mathscr{F}}$. In the case of $\tilde{\mathscr{F}}$, this lag 1 autocorrelation is entirely governed by the temporal behavior of the U_j, whose $1/e$ value has already been evaluated as 10 days. The $1/e$ value obtained for the data maps $\mathscr{F}$ is 1.2 days. However, as has been discussed above (cf. Fig. 4), this estimate represents virtually only the noisy, high-frequency components of $\mathscr{F}$, while the statistically important oscillations are much slower. As can be inferred from Fig. 4, these slow oscillations are closely related to the variability of the U_j time series, so that an appropriate $1/e$ value for $\mathscr{F}$ will be the same as that obtained for the U_j, i.e., 10 days. Using these values, one gets $2S_R = 0.23$, which corresponds to about 70 degrees of freedom.

With this test statistic, it turns out that the fractional area which is covered by significant gridpoints is less than 5%, so that the regression model has to be rejected as not being significant. However, this negative outcome is artificial, because the correlation estimates are largely affected by the high-frequency noise components of $\mathscr{F}$, thus masking the statistically important effects. To examine this point further, we repeated the test, but using low-pass (oscillation periods from 10 days to 1 season, Blackmon and Lau (1980)) filtered data map. In this case, the appropriate $1/e$ value is estimated as 19.8 days, which in turn gives $2S_R = 0.30$, corresponding to about 40 degrees of freedom. Now, 13.0% of the reference area is covered by significant corre-

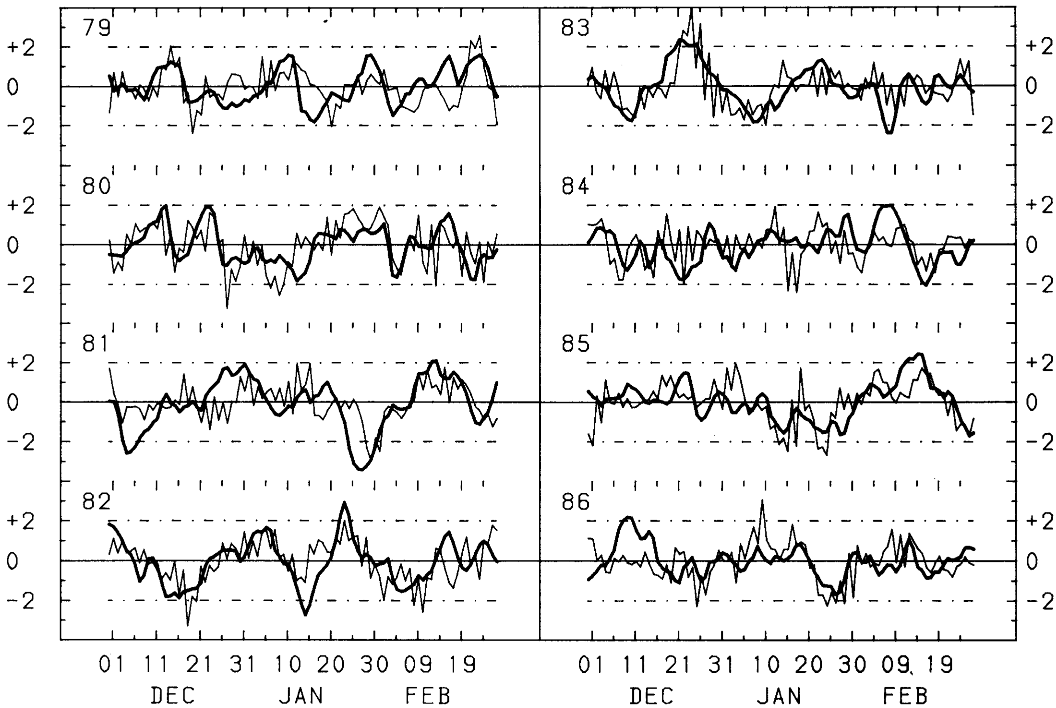

Fig. 4. Times series of U_1 (bold) and V_1 (light) as obtained for the canonical correlation analysis of Subsection 4.1.1. See text for further explanations.

lations, so that, in this case, the regression model can be accepted.

The local skill of the regression has been evaluated according to (13) using the low-pass filtered data maps and is shown in Fig. 5. One finds that the areas of significant skill are virtually confined to the Atlantic sector, with a local maximum of 25.5% near 55° N, 45° W. Some local skill is associated with the Pacific components of the canonical modes, too, but with much lower scores. Furthermore, as is evident on the basis of Fig. 5, the global skill of this regression model is very small (1.6%).

4.2. *Large-scale eddy effects*

As shown above (Figs. 1a, b), the variability of the large-scale components of the eddy effects is dominated by contributions from the Atlantic sector. Furthermore, the results of Subsection 4.1 demonstrate that the skill of the multivariate regression model is virtually confined to the Atlantic sector, too. Therefore, one might specu-

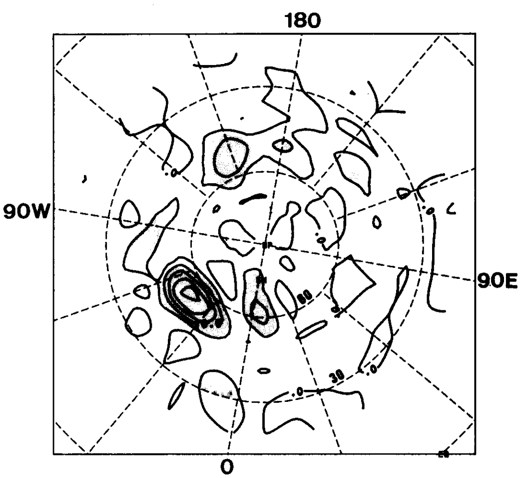

Fig. 5. Map showing the local skill (eq. (13)) of the regression model of Subsection 4.1.2 with respect to the low-pass filtered $\mathscr{F}$ maps. The contour interval is 5%. Significant areas are shaded.

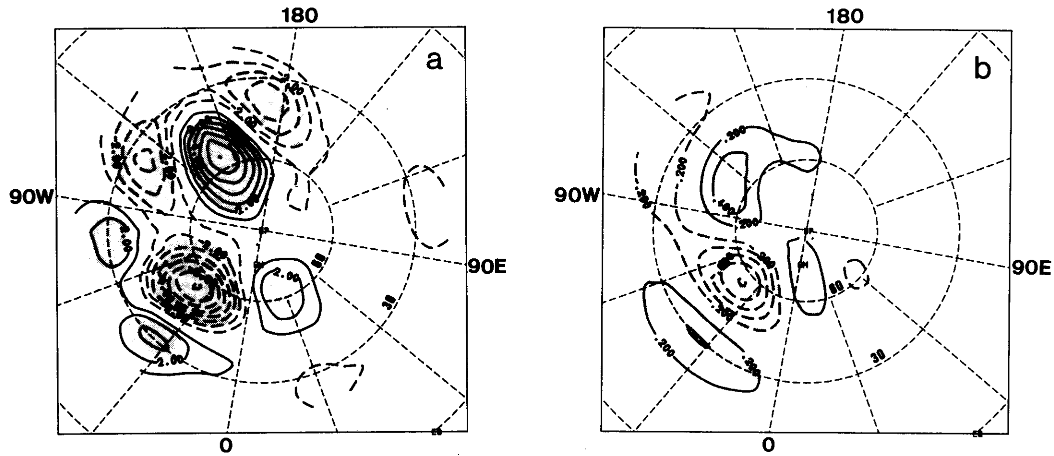

Fig. 6. As Fig. 2, but for the first canonical mode of Subsecton 4.2.1.

late that this skill originates mainly from the large-scale components of $\mathscr{F}$. To further investigate this point, we have rerun the analysis of Subsection 4.1, but using the low-order representation $\mathscr{F}_{R_4}$ instead of the total $\mathscr{F}$.

4.2.1. Canonical correlation analysis. In this case, the truncation points for the retained principal components were set to $N_F = 4$ (47.2% explained variance, cf. Table 3) for $\mathscr{F}_{R_4}$ and to $N_\psi = 9$ (48.2% explained variance) for ψ. The eigenvalues obtained from the CCA for this data are also shown in Table 4. The largest eigenvalue has about the same magnitude as that of the previous analysis. Furthermore, it is well separated from the remainder. Therefore this canonical mode is selected as the only possible candidate to be used for the regression.

Figs. 6a, b illustrate the associated canonical maps for ψ and $\nabla^{-2}\mathscr{F}_{R_4}$. Both patterns are significant with 38.6 and 42.4% of significant gridpoint area for ψ and $\nabla^{-2}\mathscr{F}_{R_4}$, respectively. It can be seen that the streamfunction pattern is rather similar over the Atlantic sector to that which has been obtained above (Fig. 2a), but the structures over the Pacific sector are entirely different. Due to the large-scale truncation, the $\nabla^{-2}\mathscr{F}_{R_4}$ pattern is now more large-scale than that of Fig. 2b, but the essential features of a dipole structure over the Atlantic are retained. As one might have expected on the basis of Fig. 1b, the pattern exhibits virtually no amplitude over the Pacific.

This partial similarity of the canonical maps has its origin in the similarity of the associated U_1 and V_1 curves, respectively. By comparing the curves obtained for the low-order case (Fig. 7) with those obtained before (Fig. 4), one can see that the curves agree rather well in nearly all their pronounced extremes.

4.2.2. Regression. The regression is performed in parallel to the previous case, by using the first canonical mode of Table 4. The data maps are now recovered from the low-order representation $\mathscr{F}_{R_4}$ of the eddy effects. In this case, the regression model turns out to be significant with respect to the unfiltered data maps, too. In particular, using $1/e$ values of 9.4 days for both the regression and the data maps, a critical value of again 0.23 is obtained for testing the correlations, and 16% of the area was covered by significant correlations. The associated pattern of the local skill values is shown in Fig. 8. It exhibits reasonable values of up to 20% over the Atlantic sector. The global skill of the regression, however, is still very small (1.5%).

The result of using the low-pass filtered $\mathscr{F}_{R_4}$ to evaluate the data maps is shown in Fig. 9. The pattern of the significant (17.8%) local skill values is virtually identical to that of Fig. 8, but the skill is higher in this case with the local maximum being 30%. Again, the global skill is very small (2.6%).

Thus, the above speculation can be confirmed and it is verified that the skill of the regression

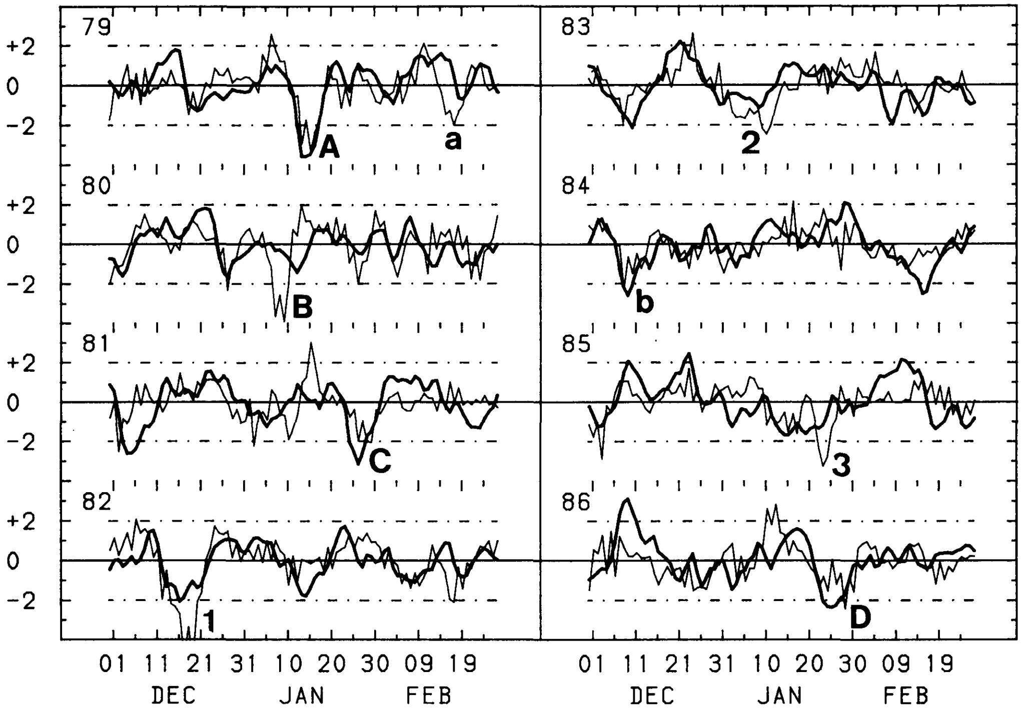

Fig. 7. As Fig. 4, but for the first canonical mode of Subsection 4.2.1. Labels A–D, a–b and 1–3 mark episodes that are used to evaluate composite maps (see Secton 5).

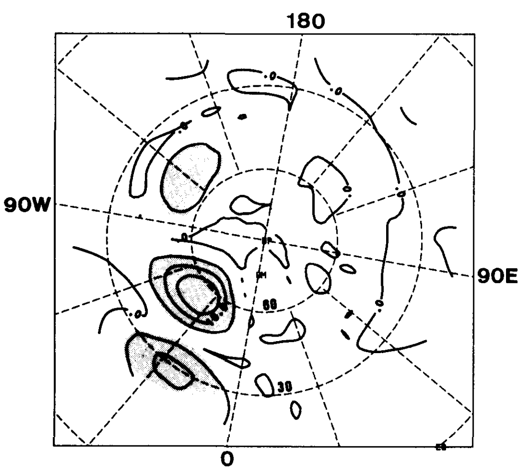

Fig. 8. As Fig. 5, but for the regression model of Subsection 4.2.2 with respect to unfiltered data maps $\mathscr{F}_{R_4}$.

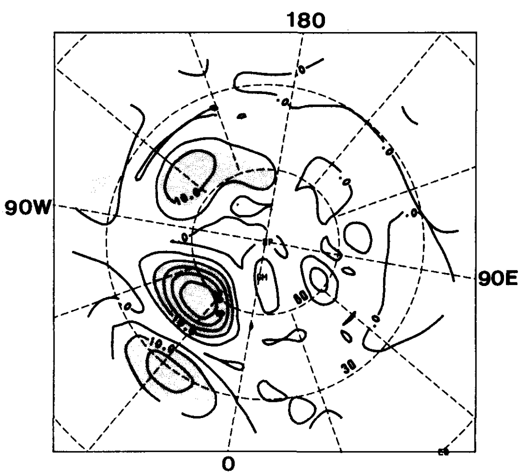

Fig. 9. As Fig. 8, but with respect to low-pass filtered data maps $\mathscr{F}_{R_4}$.

model of Subsection 4.2.1 is virtually due to large-scale effects.

5. Discussion and conclusions

We have examined the question of whether the evidence of a systematic relationship between persistent flow regimes and the barotropic effects of cyclone-scale eddies, which has been found in case studies (cf. Section 1), can be also obtained by means of a multivariate statistical analysis of hemispheric data, and furthermore, whether such a relationship also exhibits a skill in predicting the eddy effects in terms of the large-scale flow.

The results presented in Section 4 demonstrate that indeed, statistically significant regression models can be established for that purpose. In particular, it was found that the regression models exhibit some local skill (up to 30%) over the Atlantic sector, while only little skill was detected in the Pacific area. This has been explained by the finding that the skill of the regression model is almost entirely associated with the large-scale components of the eddy effects. It has been shown that the variability of these large-scale eddy effects is dominated by contributions from the Atlantic sector.

In a previous study (M89), which was carried out using low-pass filtered data, the stream-function pattern of the dominant CCA mode obtained had a similar structure but larger amplitudes over the Pacific sector than that obtained in the present study. The patterns for the barotropic eddy effects of the leading canonical modes in M89 are also similar to those obtained in the present study, but with interchanged ranking. We have re-examined the analysis of M89 and, in particular, evaluated the skill scores for the two modes (which were not computed in M89). It turns out, in agreement with the results of the present study, that the skill obtained from a regression model using the two CCA modes of M89 is entirely due to the contributions from the Atlantic sector, while the Pacific components of the CCA mode patterns exhibited virtually no skill. This again confirms our finding that the skill of the regression is mainly due to the large-scale components of the eddy effects, which are much more pronounced over the Atlantic than over the Pacific.

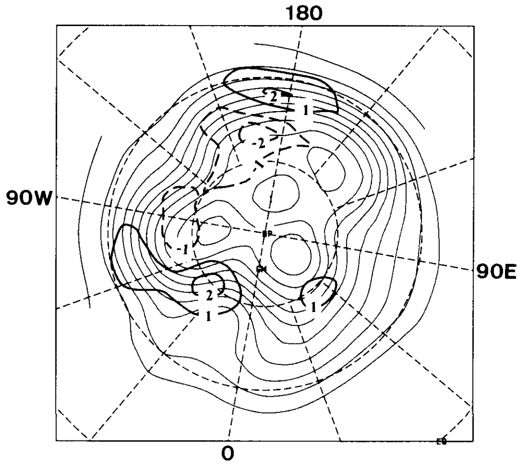

Fig. 10. Composite maps for the cases A–D of Fig. 7 of the 500 mb geopotential height (light) and the barotropic eddy effects $\nabla^{-2}\mathcal{F}$. Contour intervals are 80 gpm and $1\cdot 10^6$ m^2 s^{-1} day^{-1}, respectively. Zero lines of $\nabla^{-2}\mathcal{F}$ are suppressed.

Let us now turn to the problem of interpreting the canonical mode patterns in terms of dynamical weather regimes. To illustrate this point, we have selected episodes during which the barotropic eddy effects were particularly strong. The cases were selected from the V_1 curve in Fig. 7 as the periods (of durations of more than 5 days) during which V_1 exhibited a considerable *negative* amplitude ($|V_1|_{max} \geq 2$). 9 cases were obtained; they are marked in Fig. 7 by the labels A–D, a–b, and 1–3. The different labeling was chosen, because it turns out that the episodes are associated with different weather regimes. To illustrate these flow regimes and the associated barotropic effects of cyclone-scale eddies, composite maps for the 500 mb geopotential height and the total eddy effects were computed, whereby the raw, i.e., not detrended, data have been used.

Fig. 10 shows the composite maps for the cases A–D. One can see that these cases are associated with episodes of a classical Atlantic blocking high regime, and positive eddy induced stream-function tendencies are found at about $\frac{1}{4}$ wavelength upstream of the blocking ridge. This situation agrees with the schematic picture given by Mullen (1987) to illustrate the relationship

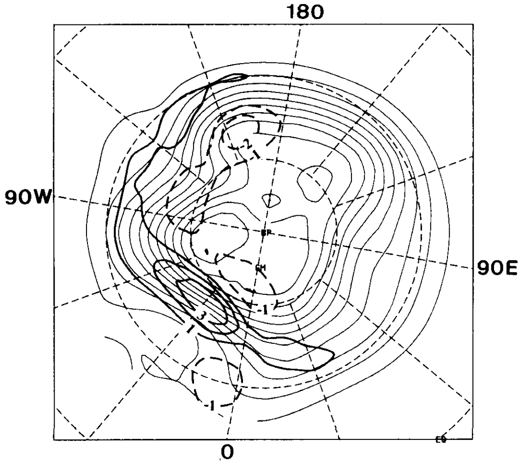

Fig. 11. As Fig. 10, but for cases 1–3 of Fig. 7.

between the net forcing of the time mean flow by the synoptic-scale eddies and the blocking wave (because the data are not detrended, the time mean eddy effect of the eddies (cf. M89, Fig. 1a) is also visible in Fig. 10 over the Pacific and the east coast of North America).

The composite maps for the cases a–b (not shown) also exhibit an Atlantic blocking high regime, but the blocking ridge is now situated further eastward over the Greenwich meridian. Again, upstream of the blocking, high positive eddy-induced streamfunction tendencies occur.

An entirely different dynamical situation is encountered with the cases 1–3 (Fig. 11). The flow over the Atlantic is governed by an anomalous strong jet northward of its normal position. In terms of the anomaly fields, this jet is due to an anomalous subtropical high to the south of it. The jet has associated with it very strong positive eddy effects tending to strengthen its northward branch and to weaken the southward branch. This situation agrees well with the schematic picture given by Hoskins (1983) to illustrate the "relationship between a time mean jet and the cyclone-scale eddy-implied forcing of the mean horizontal circulation".

Thus, the composite maps demonstrate that indeed, very different dynamical situations may contribute to a canonical mode. It is therefore at this point appropriate to discuss the limitations of our analysis technique. The major limitation has its origin in the limited data sample that is available for the analysis. Because the slow components of the large-scale atmospheric flow, which include, e.g., blocking regimes as well as anomalous jets, occur over different geographical locations, a large number of canonical modes are needed to adequately resolve this spatial variability. However, in order to obtain a larger number of significant canonical modes than in the present study, considerably more data are required to increase the degrees of freedom of the analysis. Unfortunately, at present, more data are not available.

Finally, let us return to the problem of using the technique described in the present paper as a parameterization scheme for low-order models. In this respect, it is encouraging that we have found that the skill of the regression model turns out to be mainly due to the large-scale eddy effects, so that in principle, the method might be applicable. However, the limitations discussed above, due to the sparseness of the data sample, appear at present to prohibit such an application.

6. Acknowledgements

The author is grateful to A. W. Robertson for stimulating discussions and also for a careful reading of the manuscript. This work has been supported by the German Federal Ministry of Research and Technology.

8. Appendix A

Testing correlation maps

The statistical tests used in this study mainly concern the evaluation of the significance of a map of gridpoint correlations. Such correlation maps arise in the case of the canonical maps (Subsection 2.1), which are, for testing the pattern significance, divided by the local standard deviations of the physical variable, and in connection with determining the significance of the regression model (Subsection 2.3).

The test is performed by evaluating the local significance at each gridpoint and computing then the fractional area covered by significant gridpoints. For the local test, the empirical standard deviation of the correlation coefficient is estimated (cf. Metz, 1986):

$$S_R = \{N/2 \ln[r_x^{-1}(1)\, r_y^{-1}(1)]\}^{-1/2}. \tag{A1}$$

By (A1), the degrees of freedom are implicitly determined in terms of the log 1 autocorrelations of the two time series. In the case of a spatially-dependent variable, the latter is estimated as the lag 1 value of its pattern correlation, using the spectral data.

The one variable (the cyclone-scale eddy flux convergence $\mathscr{F}$), which is under consideration in this paper, exhibits pronounced regional maxima and there are regions where it virtually disappears. Therefore, the reference area, which is used to evaluate the global significance, has been restricted to only a fraction (0.4) of the northern hemisphere. This reference area is shown in Fig. 1a. It coincides closely with the region where the standard deviation of $\mathscr{F}$ exceeds 10^6 m^2 s^{-1} day^{-1}.

As discussed by Livezey and Chen (1983), the threshold value for the fractional area should be above 5% to obtain a 95% significance, depending on the spatial degrees of freedom of the data. In our case, the latter are given by the spectral truncations, whereby the T21 and R04 truncations exhibit 231 and 35 spatial degrees of freedom, respectively. In that case, the threshold values reported by Livezey and Chen are about 7.5 and 13.5%, respectively.

REFERENCES

Austin, J. F. 1980. The blocking of middle westerly winds by planetary waves. *Quart. J. Roy. Met. Soc. 108*, 327–350.

Barnett, T. P. and Preisendorfer, R. W. 1987. Origins and levels of monthly and seasonal forecast skill for United States surface air temperatures determined by canonical correlation analysis. *Mon. Wea. Rev. 115*, 1825–1850.

Blackmon, M. L. 1976. A climatological spectral study of the 500 mb geopotential height of the northern hemisphere. *J. Atmos. Sci. 33*, 1607–1623.

Blackmon, M. L. and Lau, N.-C. 1980. Regional characteristics of the northern hemisphere wintertime circulation: a comparison of the simulation of a GFDL general circulation model with observations. *J. Atmos. Sci. 37*, 497–514.

Dole, R. M. 1986a. The life cycles of persistent anomalies and blocking over the North Pacific. *Adv. Geophys. 29*, 31–70.

Dole, R. M. 1986b. Persistent anomalies of the extratropical Northern Hemisphere wintertime circulation: structure. *Mon. Wea. Rev. 114*, 178–207.

Egger, J. and Schilling, H. D. 1983. On the theory of the long-term variability of the atmosphere. *J. Atmos. Sci. 40*, 1073–1085.

Egger, J. and Schilling, H. D. 1984. Stochastic forcing of planetary scale flow. *J. Atmos. Sci. 41*, 779–788.

Holopainen, E. O. and Fortelius, C. 1987. High-frequency transient eddies and blocking. *J. Atmos. Sci. 44*, 1632–1645.

Hoskins, B. J. 1983. Modelling of the transient eddies and their feedback on the mean flow. In: *Large-scale dynamical processes in the atmosphere* (eds. B. Hoskins and R. Pearce). New York: Academic Press.

Hotelling, H. 1936. Relations between two sets of variates. *Biometrica 28*, 321–377.

Illari, L. and Marshall, J. C. 1983. On the interpretation of eddy fluxes during a blocking period. *J. Atmos. Sci. 40*, 2232–2242.

Livezey, R. E. and Chen, W. 1983. Statistical field significance and its determination by Monte Carlo techniques. *Mon. Wea. Rev. 111*, 46–59.

Metz, W. 1986. Transient cyclone-scale vorticity forcing of blocking highs. *J. Atmos. Sci. 43*, 1467–1483.

Metz, W. 1987. Transient eddy forcing of low-frequency atmospheric variability. *J. Atmos. Sci. 44*, 2429–2439.

Metz, W. 1989. Low-frequency anomalies of atmospheric flow and the effects of cyclone-scale eddies: a canonical correlation analysis. *J. Atmos. Sci. 46*, 1026–1041.

Mullen, S. L. 1987. Transient eddy forcing of blocking flows. *J. Atmos. Sci. 44*, 3–22.

Preisendorfer, R. W., Zwiers, F. W. and Barnett, T. P. 1981. Foundations of principal component selection rules. Scripps Inst. of Oceanography, Reference series 84-4. University of California, 192 pp.

Shutts, G. J. 1986. A case study of eddy forcing during an Atlantic blocking episode. *Adv. Geophys. 29*, 135–162.